the scatterer, we have no appreciable geometrical bias. We used for B the largest angle actually observed, 15 deg. We have not considered the proton form factor in calculating these moments. In Table II, we compare these moments with the elementary-scattering distribution moments calculated from the data, using expression (7) to calculate the effective number of collisions. It gives $n=4.09\times10^6$. Also, in Table II the ratios

$$\frac{\langle\omega^4\rangle}{\langle\omega^2\rangle}=\frac{\langle\phi_2^4\rangle-\langle\phi_1^4\rangle-3\langle\phi_2^2\rangle^2+3\langle\phi_1^2\rangle^2}{\langle\phi_2^2\rangle-\langle\phi_1^2\rangle} \tag{16}$$

and

$$\frac{\langle\omega^6\rangle}{\langle\omega^2\rangle}=\frac{\langle\phi_2^6\rangle-15\langle\phi_2^4\rangle\langle\phi_2^2\rangle+30\langle\phi_2^2\rangle^3-\langle\phi_1^6\rangle+15\langle\phi_1^4\rangle\langle\phi_1^2\rangle-30\langle\phi_1^2\rangle^3}{\langle\phi_2^2\rangle-\langle\phi_1^2\rangle}$$

are compared with those calculated for the two elementary distributions. These quantities are independent of the effective number of collisions.

Although some of the experimental uncertainties are comparable to the magnitude of the measured quantity, these errors are all much less than the moments predicted for a point-nucleus model. The experiment also serves very well to illustrate how the theory of moment propagation may be applied practically.

Elastic K^+-Proton Scattering at 970, 1170, and 1970 MeV/c*

V. Cook, D. Keefe, L. T. Kerth, P. G. Murphy,† W. A. Wenzel, and T. F. Zipf
Lawrence Radiation Laboratory, University of California, Berkeley, California
(Received 29 October 1962)

A liquid-hydrogen target surrounded by spark chambers was used to study K^+-proton elastic scattering at 970, 1170, and 1970 MeV/c incident K^+ momentum. In contrast with results at lower energies, the angular distributions were not isotropic; the anisotropy increases with energy, while the elastic cross section decreases. A number of phase-shift solutions using (a) $S_{1/2}$, $P_{1/2}$, and $P_{3/2}$ complex phase shifts; (b) real $S_{1/2}$, $P_{1/2}$, and $P_{3/2}$, and complex $D_{3/2}$ phase shifts; and (c) complex $S_{1/2}$ and $D_{3/2}$, and real $P_{1/2}$ and $P_{3/2}$ phase shifts have been found for the 970- and 1170-MeV/c data. The 1970-MeV/c distribution has been fitted by an optical model. The data presented here have been included with other information on K-nucleon scattering in a test of forward-scattering dispersion relations. The data are still insufficient to provide a definitive test; however, an acceptable fit was found for Γ (effective pole residue) $= -0.1\pm0.3$.

1. INTRODUCTION

PREVIOUS experiments on the interaction of K^+ mesons with nucleons include investigations at low energies of the total and elastic cross sections by means of emulsions (0 to 600 MeV/c),[1] counters (500 to 600 MeV/c),[2] the propane bubble chamber,[3] and the 15-in. Berkeley liquid-hydrogen bubble chamber (100 to 810 MeV/c).[4]

In the region above 810 MeV/c, the only data hitherto available have been total K^+-p and K^+-n cross-section measurements from counter experiments by Burrowes et al. (up to 2.5 BeV/c)[5]; von Dardel et al. (2.9 to 6 BeV/c)[6]; Vovenko et al. (2 to 4 BeV/c)[7]; Cook et al.

[1] D. Keefe, A. Kernan, A. Montwill, M. Grilli, L. Guerriero, and G. A. Salandin, Nuovo Cimento 12, 241 (1959).

[2] T. F. Kycia, L. T. Kerth, and R. G. Baender, Phys. Rev. 118, 553 (1960).

[3] D. I. Meyer, D. A. Glaser, and M. L. Perl, Phys. Rev. 107, 279 (1957).

[4] T. F. Stubbs, H. Bradner, W. Chinowsky, G. Goldhaber, S. Goldhaber, W. Slater, D. M. Stork, and H. K. Ticho, Phys. Rev. Letters 7, 188 (1961).

[5] H. C. Burrowes, D. O. Caldwell, D. H. Frisch, D. A. Hill, D. M. Ritson, and R. A. Schluter, Phys. Rev. Letters 2, 117 (1959).

[6] G. von Dardel, D. H. Frisch, D. Mermod, R. H. Milburn, P. A. Piroué, M. Vivargent, G. Weber, and K. Winter, Phys. Rev. Letters 5, 333 (1960).

[7] A. S. Vovenko, B. A. Kulakov, M. F. Lykhachev, A. L.

8" diameter
quadrupole lens
(triplets)

12" x 60"
deflecting
magnet

Proton-beam
trajectory

Internal
target

B_3
A_2
B_4

T_1
T_2

Q_3 M_3

C_2 C_1

Q_2

M_2

M_1 Q_1

B_2
A_1

B_1

Scale (ft)
0   10

2000 psi
Čerenkov
counters

13" x 24"
C magnets

48" liq. H_2
or deuterium
target

8" diameter
quadrupole lens
(doublet)
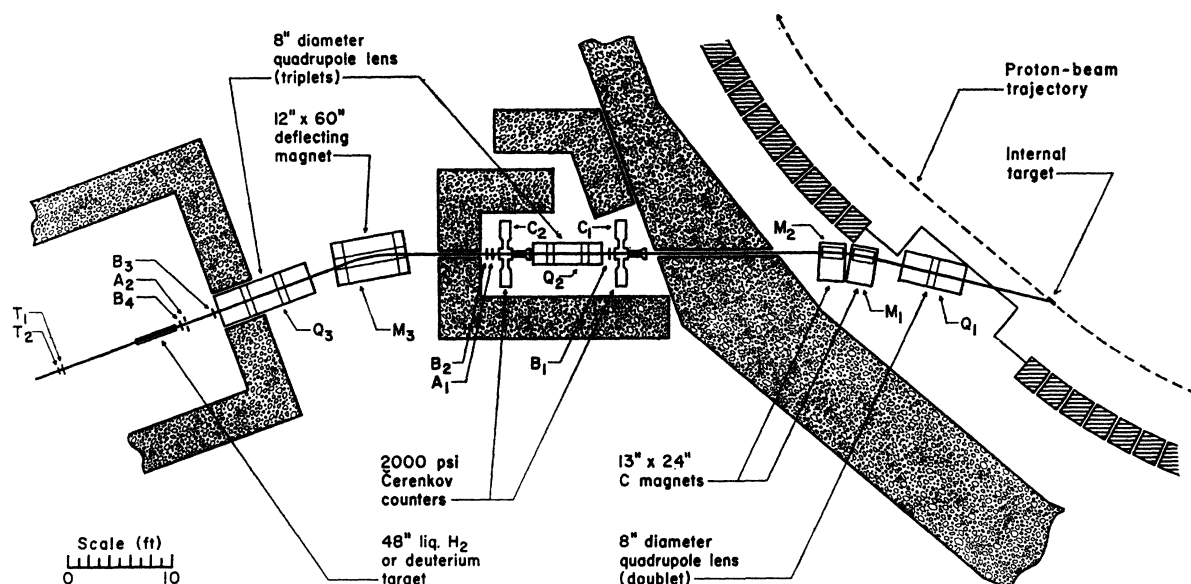
FIG. 1. Layout of K^+ beam apparatus.

(0.8 to 2.9 BeV/c)[8]; and Kycia et al. (3 to 20 BeV/c).[9]

The measurement of differential cross sections at high energies has been complicated by the small fluxes of K^+-particle beams, the difficulty of producing well-separated high-energy K^+ beams for bubble chambers, and the severe competition of decay in flight with interaction in high-resolution counter experiments. The present paper reports three measurements of elastic K^+-p scattering distributions at high energies by use of spark chambers. The good resolution time (approximately 0.5 μsec) of the spark chambers and the triggering system made possible the use of an electronically separated K^+ beam to obtain a high rate. An array of spark chambers close to the hydrogen target was used to obtain accurate angular information, large solid angle, and to minimize complications due to decay in flight. Two other experiments, one on total cross section,[8] the other on rare-particle production,[10] were carried out in the same beam and have been reported. Neither involved the use of the spark-chamber array.

2. EXPERIMENTAL DETAILS AND RESULTS

2.1 Beam Layout

The positively charged secondary beam was produced from a 4- by $\frac{1}{2}$- by $\frac{1}{4}$-in. heavymet target placed in the west straight section of the Bevatron. Particles which

were produced as close as possible to the forward direction (26 deg) and could still emerge without obstruction were selected in momentum by the beam-transport system shown in Fig. 1. The final spatial focus was also a momentum focus. The magnetic quadrupole lens Q_1 produced a horizontal and vertical image of the internal target close to the center of the field lens Q_2. The final quadrupole lens Q_3 in turn focused this image anastigmatically at the liquid-hydrogen target. The dispersion of the first pair of bending magnets M_1 and M_2 was such that the aperture stop defined by Q_2 accepted particles with momenta between $\pm 4\%$ of the central momentum. The final bending magnet M_3 served to redefine the momentum and to remove the dispersion caused by M_1 and M_2. The quadrupole field lens Q_2 was used to obtain increased flux and to improve the recombination of momenta.

The exit window in the straight section of the Bevatron was 0.020 in. thick. Apart from the space needed for counters, the beam channel was occupied by polyethylene bags containing helium, in order to reduce loss by multiple scattering.

The hydrogen target was 48 in. long and 6 in. in diameter, with 0.005-in. stainless steel walls. The vacuum vessel surrounding the hydrogen vessel had $\frac{1}{4}$-in. aluminum walls, a Mylar entrance window 0.020 in. thick, and an exit hemispherical window of aluminum $\frac{1}{16}$ in. thick.

2.2 Electronic Equipment

Particles of the correct momentum were detected by the four beam scintillation counters B_1, B_2, B_3, and B_4. The pairs B_1, B_3, and B_2, B_4 were used to select the appropriate time of flight, and were connected in sepa-

Ljubimov, Ju. A. Matulenko, I. A. Savin, Ye. V. Smirnoff, V. S. Stavinsky, Sui Yuin-Chan, and Shzan Nai-Sen, Joint Institute for Nuclear Research, Dubna Report D 721, 1961 (unpublished).

[8] V. Cook, D. Keefe, L. T. Kerth, P. G. Murphy, W. A. Wenzel, and T. Zipf, Phys. Rev. Letters 7, 182 (1961).

[9] E. W. Jenkins, W. F. Baker, R. L. Cool, T. F. Kycia, R. H. Phillips, and A. L. Read, Bull. Am. Phys. Soc. 6, 433 (1961).

[10] V. Cook, D. Keefe, L. T. Kerth, P. G. Murphy, W. A. Wenzel, and T. F. Zipf, Phys. Rev. 123, 655 (1961).

rate coincidence circuits. The methane-gas Čerenkov counters C_1 and C_2 have been fully described previously,[11] and have an optical system which detects separately the Čerenkov light from K mesons and π mesons of the same momentum. Because of the design upper limit on pressure (2000 psi), this mode of operation is possible only for momenta above 1.3 BeV/c, for which K mesons produce sufficient Čerenkov radiation. Below 1.3 BeV/c the counters were used purely in anticoincidence to reject π mesons. Thus, at 970 and 1170 MeV/c, π mesons were rejected by anticoincidence and protons by time of flight. At 1970 MeV/c, in addition to the π anticoincidence and the time-of-flight selection, K-meson identification in the appropriate channels in both Čerenkov counters was required. The contamination in all the K^+ beams discussed here was less than 0.1%. Figure 2 shows the fluxes of protons, kaons, and pions as functions of momentum for an internal proton-beam energy of 5.5±0.5 BeV. In producing a high-flux K-meson beam (approximately 300 per pulse) the accidental rate due to the several hundred thousand accompanying particles poses certain problems. In an experiment using a similar beam with K^- mesons,[12] attention was drawn to the fact that the accidental rate due to π^- mesons was reduced by at least two orders of magnitude, because the anticoincidence pulse was longer by a substantial factor than the resolving time of the fast K-coincidence circuits. The case of the positive beam discussed here was more complicated. The π^+ mesons were rejected by anticoincidence signals from C_1 and C_2. However, the protons were not detected by these counters, so elimination of proton accidentals was more difficult. As can be seen from Fig. 2, the number of protons in the beam exceeded the number of π^+ at all but the lowest momentum. As a general solution, independent of the nature of the accidental particle, a special stretching and adding circuit was used to reject from consideration any K^+ meson if another particle passed through the system closer in time than ±50 nsec. Each pulse from a 5- by 5- by $\frac{1}{2}$-in. beam scintillator A_1 (see Fig. 1) was shaped by a delay-line stretcher to produce a 50-nsec rectangular pulse. Thus, if two particles passed through A_1 within 50 nsec of each other, the region of overlap of the stretched pulses gave a signal of twice the normal height. A discriminator set to select such double-event signals provided the required anticoincidence signal.

2.3 Hodoscope Equipment

The hodoscope system for momentum and velocity analysis shown in Fig. 3(a) recorded K^+-p elastic scattering close to the forward direction. Except for a slight

[11] B. Cork, D. Keefe, and W. A. Wenzel, in *Proceedings of International Conference on Instrumentation for High Energy Physics, Berkeley, 1960* (Interscience Publishers, Inc., New York, 1961), p. 84.
[12] V. Cook, Bruce Cork, T. F. Hoang, D. Keefe, L. T. Kerth, W. A. Wenzel, and T. F. Zipf, Phys. Rev. **123**, 320 (1961).
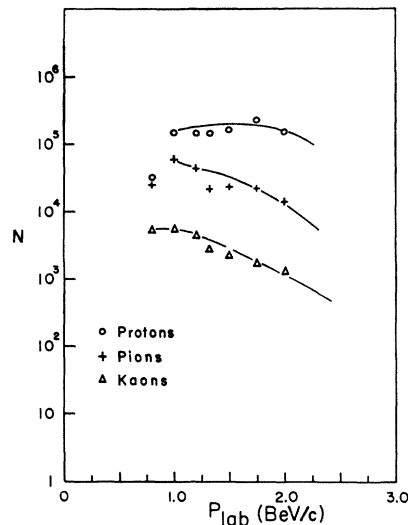

FIG. 2. The composition of the beam given in terms of the number of particles per 10^{11} protons incident on a 4-in. heavymet target per 1.5 msr, and for a momentum spread $\Delta p/p = 0.08$. Rates measured at about 90 ft from the production target were corrected for decay in flight and absorption in the Čerenkov counters to deduce the approximate production rates. The production angle was 26°.

change in the geometrical configuration, the arrangement is identical with that used in the K^--p scattering experiment by Cook *et al.*[12] The hodoscope scintillation counters in H_1, H_2, and H_3 are all 8 in. high, 3 in. wide, and $\frac{1}{4}$ in. thick. The elements in H_1 and H_2 are overlapped to yield 1-in. horizontal resolution. The pressure in the sulfur-hexafluoride-gas Čerenkov counter (vertical aperture of 10 in., horizontal aperture of 48 in.) was set just below the threshold pressure required to count the K mesons in the beam. The signal from this counter was placed in anticoincidence to reject any forward π's, μ's, or electrons from K mesons decaying in the hydrogen target, or between the target and the last hodoscope. The pulses from each of the hodoscope elements were placed in coincidence in independent two-channel diode circuits with a "K gate" pulse, and the outputs of these were displayed in time sequence on a recording oscilloscope.

The pole faces and inner surfaces of the copper coils of the analyzing magnet were lined with anticoincidence scintillation counters ($\frac{3}{8}$ in. thick) to reject particles that struck the magnet and scattered into the final hodoscope array. Although such events could have been rejected after scanning by the constraints on the H_1, H_2, and H_3 coordinate positions, they would have produced a rather large number of spurious triggers.

From the coordinates of the scattered particle at the three positions H_1, H_2, and H_3, the momentum, angle of scattering, and origin of any scattered particle were determined. Background contamination was removed by running with the hydrogen target alternately full and empty, then making a suitable subtraction. The hodoscope system measured the differential cross section for
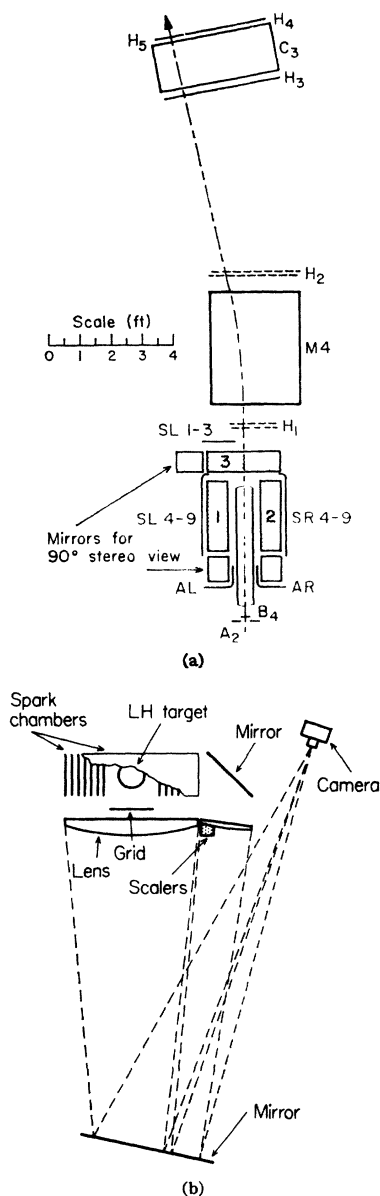
FIG. 3. (a) Plan view of apparatus used to detect scattered particles; (b) Elevation view of spark-chamber setup.

angles in the region $\theta_{lab} \approx 4$ to 13 deg, corresponding to $\theta_{c.m.} \approx 8$ to 25 deg.

2.4 Hodoscope Results

About 10 000 oscilloscope sweeps were obtained at each of the primary momenta. Electronic pickup from the spark-chamber trigger pulses caused about one-half the total number of traces, and these were easily rejected by inspection. About two-thirds of the remaining traces fitted the elastic-scattering criteria. That is, the coordinates of the particle measured at H_1, H_2, and H_3 [see Fig. 3(a)] were consistent with a scattering vertex

in the hydrogen target and a momentum within about 10% of that expected for an elastically scattered K particle. In a momentum-distribution plot these events stood out in a strong peak above a broad background. Most of the background events were due to decays in flight between H_2 and H_3. However, despite the acceptable kinematical fit, a "target full" minus "target empty" subtraction was necessary, since there were some acceptable elastic-scattering events in the "target empty" runs. Almost all of these arose from scattering in the aluminum end window of the target. The ratio of the numbers of scatters per incident K meson in the full and empty runs was approximately five to one. In the final analysis, the forward-scattering measurements were based on approximately 140 events at 970 MeV/c, 270 events at 1170 MeV/c, and 750 events at 1970 MeV/c.

It is important to notice that, in contrast to the previous application[12] of this equipment to measure K^--p diffraction scattering, only the sum of the forward ($\theta_{c.m.} \approx 0$ deg) and backward ($\theta_{c.m.} \approx 180$ deg) cross sections could be determined in the case of a positive K-meson beam. (The recoil proton from a K^+ meson scattered backwards bends in the same direction and approximately the same amount in the analyzing field as a K^+ meson scattered in the forward direction.) Thus, the rate in the hodoscope experiment determined

$$A\frac{d\sigma}{d\Omega}(\theta_{lab}{}^K = \theta) + B\frac{d\sigma}{d\Omega}(\theta_{lab}{}^p = \theta),$$

where A and B depend on the relative efficiencies for detecting K mesons and protons. We found that we could accurately calculate the attenuation factors due to the interaction or scattering of the K^+ mesons and protons in the hydrogen target and aluminum vacuum vessel, and the loss of the K^+ mesons due to decay in flight. The partition between forward and backward scattering was determined by extrapolation of the spark-chamber data in the backward direction to determine the average value of $d\sigma/d\Omega$ near $\theta_{c.m.}{}^K = 180$ deg. The errors arising from this extrapolation and from the subtraction were small compared with the statistical errors, and are included in the uncertainties quoted later.

2.5 Spark-Chamber Equipment

Figures 3(a) and 3(b) show the arrangement of the three rectangular parallel-plate spark chambers used to measure $d\sigma/d\Omega$ at large angles ($\theta_{c.m.} \gtrsim 30$ deg). The hollow plates in each chamber were 10 in. wide by 28 in. long, and were made by stretching aluminum 0.003-in. foil over a picture frame of 1-in.-diam aluminum pipe.

The outer electrodes were 0.012-in. aluminum sheet fastened to a flat frame. The five hollow plates and two outer sheets were mounted so as to provide six parallel gaps each of $\frac{3}{4}$-in. spacing.

TABLE I. Summary of the recorded spark-chamber data.

Momentum (MeV/c)	970		1170		1970	
Target	Full	Empty	Full	Empty	Full	Empty
No. of pictures	3706	284	5766	447	11 783	1456
No. of K^+(10^6)	0.796	0.161	1.133	0.360	2.582	0.593
No. of elastic K^+-p scatters accepted	1261	0	1699	0	1593	1

Two 90-deg stereo views of each chamber were obtained by tilted mirrors as shown. To obtain unobscured views throughout the full depth of every gap a Lucite field lens ($f = 15$ ft) was used and the camera placed at its focus [see Fig. 3(b)]. One surface of the lens was plane; the other was hyperboloidal to eliminate spherical aberration. An illuminated Lucite reference grid, ruled in 1-in. squares, covered the plan view of the hydrogen target. The film was advanced by one frame between Bevatron pulses; a maximum of one picture was taken per pulse. Each picture included an image of remotely located scalers [see Fig. 3(b)] which recorded the number of K^+ mesons appropriate for normalization.

At the beginning of each Bevatron pulse an "on" gate was started, which permitted a scaler to record the number of K^+ mesons entering the hydrogen target and enabled operation of the spark-chamber trigger circuit. When an interaction occurred, a spark-chamber trigger was generated and the gate was turned off. For the remainder of that pulse the scaler and the spark-chamber trigger circuit were thus gated off, so that the scaler gave the correct normalization for the calculation of the cross section. However, as a check, the total number of K^+ mesons and the total number of interactions occurring per pulse were recorded on separate scalers that did not involve the "off" gate feature. Since the recording oscilloscope could photograph many traces per pulse, all K^+ mesons were accepted as possible scattering candidates in the hodoscope system. The signal indicating an interaction in the hydrogen target was provided by a coincidence between the group of scintillators to the left of the target, S_L, and the group to the right, S_R [Fig. 3(a)].

The spark chambers were evacuated initially and filled with argon at atmospheric pressure. The high-voltage pulse of 20 kV was derived from two 5949 hydrogen thyratrons with a pre-stage comprising an EFP60 secondary emission tube and a 6130 thyratron. A small dc clearing field was applied to the electrodes to sweep out the ions formed by the passage of particles in the main beam. The magnitude (40 V) and sign (opposite to the high-voltage pulse) were chosen to minimize the number of accidental tracks without any significant loss in sparking efficiency per gap. The resolution time of the chambers under these conditions was about 500 nsec. The length of this time is dominated by the interval required to complete the electronic logic needed to generate a trigger pulse (300 nsec).
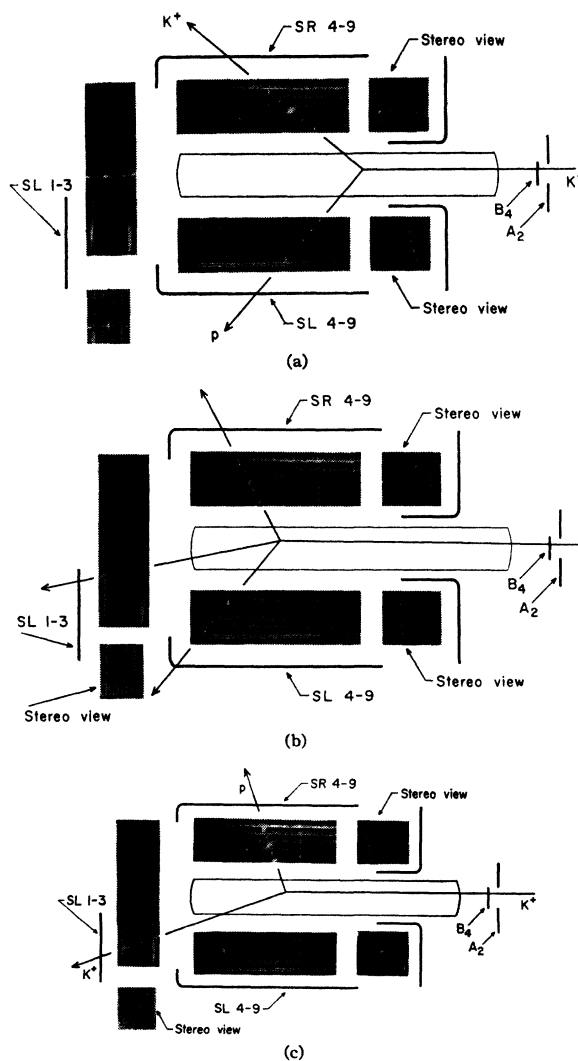

FIG. 4. Composites made from typical spark-chamber photographs. (a) Elastic "side-side" scatter; (b) Inelastic scatter; (c) Elastic "front-side" scatter.

In scanning for elastic scattering events, two classes of events could be distinguished: those where one particle entered the left-hand chamber, and the other the right-hand chamber; and those where one particle entered the forward chamber. In the first case, the end-mirror views provided a beam's-eye view and the constraint of coplanarity reduced to the requirement that the images be closely collinear [compare Figs. 4(a) and 4(b)]; it was thus possible by inspection to reject noncoplanar events rapidly. In the second case [cf. Fig. 4(c)] no such simple criterion was possible, and the correlation of all sets of images had to be made before deciding whether the event was coplanar.

2.6 Spark-Chamber Results

Table I summarizes the quantities of spark-chamber photographs taken at the three momenta, the quantities

Table II. Differential cross sections in K^+-p c.m. system, measured with the spark-chamber apparatus.

| | Momentum (MeV/c) | | | | | | | |
| | 970 | | | 1170 | | | 1970 | | |
cosθ*	$\frac{d\sigma}{d\Omega}$ (mb/sr)	Δσcorr[a]	cosθ*	$\frac{d\sigma}{d\Omega}$ (mb/sr)	Δσcorr[a]	cosθ*	$\frac{d\sigma}{d\Omega}$ (mb/sr)	Δσcorr[a]
0.76±0.06	1.07±0.18	0.53	0.78±0.08	1.89±0.24	1.09	0.92±0.02	1.52 ±0.21	0.69
0.6 ±0.10	0.84±0.09	0.22	0.65±0.05	1.26±0.14	0.32	0.85±0.05	1.84 ±0.15	0.39
0.4 ±0.10	1.15±0.11	0.27	0.55±0.05	1.19±0.12	0.33	0.75±0.05	1.47 ±0.14	0.31
0.15±0.15	0.75±0.07	0.17	0.45±0.05	0.95±0.10	0.21	0.65±0.05	1.04 ±0.11	0.22
−0.1 ±0.10	0.57±0.06	0.13	0.35±0.05	1.04±0.10	0.30	0.55±0.05	0.49 ±0.06	0.09
−0.3 ±0.10	0.67±0.08	0.17	0.15±0.15	0.61±0.05	0.14	0.45±0.05	0.44 ±0.06	0.08
−0.5 ±0.10	0.76±0.10	0.22	−0.05±0.05	0.42±0.05	0.09	0.35±0.05	0.32 ±0.05	0.06
−0.7 ±0.10	0.67±0.09	0.21	−0.15±0.05	0.35±0.05	0.08	0.25±0.05	0.27 ±0.04	0.05
−0.88±0.08	0.61±0.11	0.27	−0.25±0.05	0.33±0.05	0.08	0.10±0.10	0.12 ±0.06	0.02
			−0.35±0.05	0.36±0.06	0.08	−0.05±0.05	0.061±0.023	0.011
			−0.45±0.05	0.43±0.07	0.12	−0.15±0.05	0.083±0.028	0.016
			−0.55±0.05	0.24±0.05	0.07	−0.25±0.05	0.056±0.021	0.011
			−0.65±0.05	0.41±0.07	0.13	−0.35±0.05	0.029±0.014	0.006
			−0.75±0.05	0.36±0.06	0.11	−0.45±0.05	0.048±0.016	0.011
			−0.85±0.05	0.43±0.07	0.14	−0.55±0.05	0.054±0.016	0.013
			−0.93±0.03	0.73±0.17	0.28	−0.65±0.05	0.064±0.017	0.015
						−0.75±0.05	0.062±0.017	0.016
						−0.85±0.05	0.081±0.019	0.021
						−0.94±0.04	0.043±0.021	0.013

[a] The listed cross sections include this correction, which is the sum of the corrections for stopping proton loss, proton interaction, and K decay and interaction.

eventually selected as elastic scattering events, and the corresponding quantities of K^+ mesons entering the hydrogen target within the "on" gate time. All events with two outgoing tracks were measured if the projected opening angle was greater than 70 deg (the minimum projected opening angle for an elastic scattering was greater than 80 deg). The angles of the two tracks with respect to the fiducial grid lines were measured in both stereo views on the projection scanning table. The typical uncertainty in measurement was between 0.5 and 1 deg. The scanners recorded the angles and the coordinates of the vertex directly on IBM punched cards. An IBM 650 was used to compute the space angles and compare them with the expected values for elastic scattering. The program contained no kinematical fitting routine, but was simply used to obtain a print out of the deviation of each event from (a) coplanarity, and (b) elastic kinematics. The expectation values of these deviations were dependent on scattering angle, being worst for scatterings close to the forward and backward directions. Both distributions were simultaneously sharply peaked about zero, and a realistic cutoff was easy to apply; the errors in the number of accepted elastic-scattering events arising from uncertainty in the cutoff was at most 5% for c.m. scattering angles close to 0 and 180 deg, and 2% for the bulk of the events. These errors were included in the final uncertainty estimates but in reality were almost negligible compared with the statistical errors.

Because the vertex of each event could be located accurately, events originating in the liquid hydrogen were easily discernible and, as Table I makes clear, there was little need to take alternate full and empty target data. The events rejected as nonelastic comprised inelastic interactions in the hydrogen and interactions in the aluminum vacuum vessel. The relatively small solid angle subtended by the spark chambers did not make it worthwhile to attempt an analysis of the inelastic K^+-p interactions.

Certain corrections, amounting typically to less than 10%, were applied. These included corrections for events lost or rejected either because the K meson decayed in flight before passing through the spark chamber or because the proton or K^+ interacted in the hydrogen or vacuum vessel. Apart from the high angular resolution obtained, a major advantage of using spark chambers as detectors in close proximity to the hydrogen target was the reduction of the decay-in-flight correction from a large factor to a reasonably small correction.

3. ANALYSIS AND DISCUSSION OF RESULTS

Tables II and III show a list of the final corrected differential cross sections obtained, together with the magnitudes of the corrections that have been added to the observed numbers. The errors shown include the effects due to statistical fluctuations and uncertainties in the corrections. These results and the hodoscope results are shown in Figs. 5(a), 5(b), and 5(c). The total elastic cross sections, shown in Table IV, were obtained by integrating beneath the experimental curves. The variation of σ_e and σ_T with energy is shown in Fig. 6.

3.1 The 970- and 1170-MeV/c Data

Stubbs et al.[4] have measured the differential cross section for K^+-p at 810 MeV/c, and have found an almost isotropic distribution. The simplest hypothesis

TABLE III. Differential cross sections in the c.m. system, measured with the hodoscope apparatus.

1970 MeV/c			1170 MeV/c			970 MeV/c		
θ^*	N[a]	$\dfrac{d\sigma}{d\Omega}$ (mb/sr)	θ^*	N[a]	$\dfrac{d\sigma}{d\Omega}$ (mb/sr)	θ^*	N[a]	$\dfrac{d\sigma}{d\Omega}$ (mb/sr)
8.1	153±38	5.21±1.29	9±2	150±41	3.36±0.92	15±8	92±30	2.40±0.78
10.7	117±30	4.36±1.12	20±5	120±21	2.36±0.45			
13.3	119±23	3.94±0.80						
15.8	80±17	2.62±0.56						
18.3	81±14	2.62±0.45						
20.7	62±14	2.08±0.47						
23.1	57±14	1.94±0.48						
25.4	48±8	2.08±0.41						
27.7	39±7	2.41±0.43						
29.8	23±6	2.75±0.72						

[a] The net number of elastic scatters after the full-empty subtraction.

is that S-wave scattering dominates (solution A of reference 3), but these authors also find satisfactory fits with a dominant $P_{1/2}$ solution (solution B: Minami transform of A) or a combination of $P_{1/2}$ and $P_{3/2}$ amplitudes (solution C: Fermi-Yang ambiguity corresponding to solution B). Other measurements at lower momenta[1-4] are consistent with the hypothesis that the scattering is pure S wave. Our observed distributions at 970 and 1170 MeV/c show that the elastic-scattering cross section is still large at all angles, but that the departure from isotropy becomes increasingly marked with rising energy.

Because of the large inelastic cross section it is necessary that at least one of the phase shifts be complex.

It is obvious that the almost pure S-wave behavior up to 810 MeV/c does not continue up to 970 MeV/c, hence the following choice of sets of phase shifts was made:

Set (a): $S_{1/2}$, $P_{1/2}$, and $P_{3/2}$ phase shifts, all complex: This assumed that only the next higher waves $P_{1/2}$ and $P_{3/2}$ would be needed. Thus, there were six parameters to be fitted to the data.

Set (b): $S_{1/2}$, $P_{1/2}$, and $P_{3/2}$ all real; $D_{3/2}$ complex: If one assumes that pion production proceeds mainly through the reaction

$$K+p \to K+N^* \to K+N+\pi$$
(threshold $p_K = 880$ MeV/c),
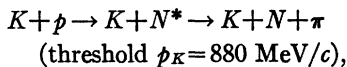
at 970 MeV/c, where the final KN^* system is largely in an S-wave state, then the absorption should be confined to the $D_{3/2}$ state. Thus, the choice of solution of this type, albeit with only five parameters compared to the six of set (a), would be expected to provide a good fit.

Set (c): $P_{1/2}$, $P_{3/2}$ real; $S_{1/2}$, $D_{3/2}$ complex: At 1170 MeV/c, pion production can occur through the reactions

$$K+p \to K+N^* \to K+N+\pi,$$
and
$$K+p \to K^*+N \to K+N+\pi$$
(threshold $p_K = 1060$ MeV/c).
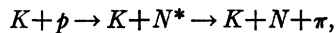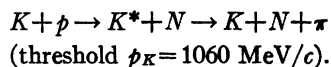
If we assume that the final states are mainly S-wave and

the spin of K^* (mass 888 MeV) is one, absorption due to the second process should occur in the $D_{3/2}$ or $S_{1/2}$ channels; hence the choice of this set.

The scattering cross section equation used in fitting the 970- and 1170-MeV/c data (including both Coulomb and nuclear effects) was written:

$$d\sigma/d\Omega = |A|^2 + |B|^2 \sin^2\theta.$$

The nonflip amplitude is

$$A = -\frac{\lambda n}{2\sin^2(\theta/2)} \exp[-in \ln \sin^2(\theta/2)]$$

$$+ (\lambda/2i)\{\eta_0 \exp(2i\alpha_0) + [2\eta_1^+ \exp(2i\alpha_1^+)$$

$$+ \eta_1^- \exp(2i\alpha_1^-) - 3 \exp(2i\phi_1)] \cos\theta$$

$$+ [3\eta_2^+ \exp(2i\alpha_2^+) + 2\eta_2^- \exp(2i\alpha_2^-)$$

$$- 5 \exp(2i\phi_2)]\tfrac{1}{2}(3\cos^2\theta - 1)\},$$

and the spin-flip amplitude is

$$B = \frac{\lambda n C \sin\theta}{2\sin^2(\theta/2)}$$

$$+ \frac{\lambda}{2i}\{[\eta_1^+ \exp(2i\alpha_1^+) - \eta_1^- \exp(2i\alpha_1^-) - \tfrac{3}{2}nC]$$

$$+ [\eta_2^+ \exp(2i\alpha_2^+) - \eta_2^- \exp(2i\alpha_2^-) - \tfrac{5}{8}nC]3\cos\theta\},$$

where λ = the particle wavelength in the c.m. system,

TABLE IV. Elastic (σ_e) and total (σ_T) cross sections for K^+-p.

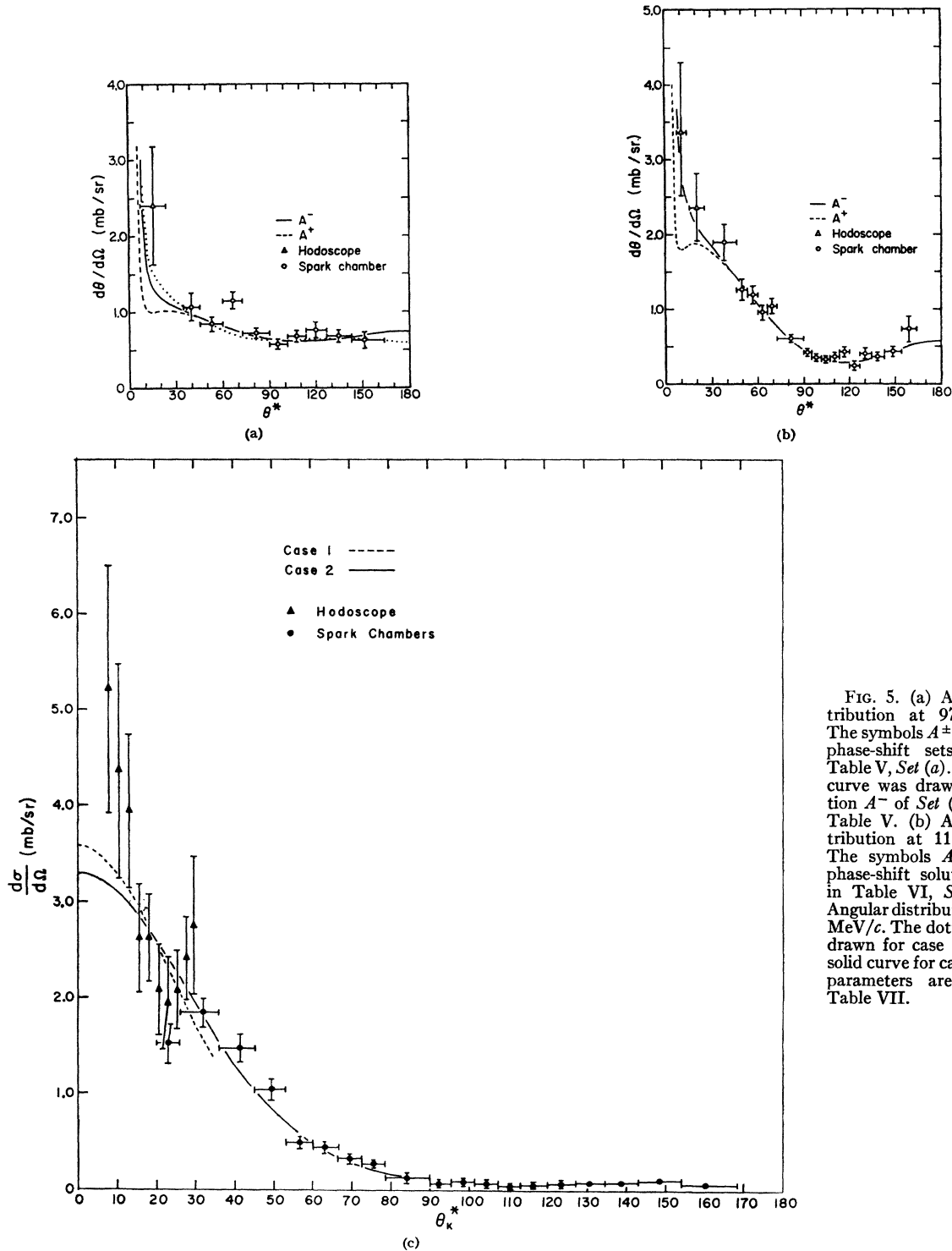| Momentum (MeV/c)	800	970	1170	1970	Reference
σ_e (mb)	12.2±0.4	···	···	···	Stubbs et al.[a]
	···	10.2±1.5	10.7±1.1	5.6±0.4	This experiment
σ_T (mb)	13.2±0.5	···	···	···	Stubbs et al.[a]
	13.0±0.9	15.4±0.6	18.1±0.6	16.9±0.4	Cook et al.[b]

[a] Reference 4.
[b] Reference 8.

(a)

(b)

(c)

FIG. 5. (a) Angular distribution at 970 MeV/c. The symbols $A^\pm$ refer to the phase-shift sets given in Table V, Set (a). The dotted curve was drawn for solution A^- of Set (b) given in Table V. (b) Angular distribution at 1170 MeV/c. The symbols $A^\pm$ refer to phase-shift solutions given in Table VI, Set (a). (c) Angular distribution at 1970 MeV/c. The dotted curve is drawn for case (i) and the solid curve for case (ii). The parameters are given in Table VII.

θ = scattering angle in the c.m. system, and $n = e^2/\hbar c(\beta_K)_{\rm lab}$. The complex phase shifts have been written, for $j = l \pm \frac{1}{2}$,

$$\delta_l^\pm = a_l^\pm + i\beta_l^\pm,$$

$$\eta_l^\pm = \exp(-2\beta_l^\pm).$$

The quantity C is the result of a first-order relativistic correction to the Coulomb scattering amplitude[13]:

$$C = \frac{\frac{1}{2}\mu_P \beta_K \beta_P + (\frac{1}{2}\mu_P - \frac{1}{4})\beta_P^2}{1 + \beta_K \beta_P},$$

[13] F. T. Solmitz, Phys. Rev. 94, 1799 (1954).

Table V. Phase-shift solutions found at 970 MeV/c.

Set (a)	δ_0	η_0	δ_1^-	η_1^-	δ_1^+	η_1^+	$D(f)$	$P(\chi^2)$
A^-	-38 ± 1	1.0	-10 ± 1	1.0	3 ± 4	0.6	-0.10 ± 0.03	0.14
A^+	39 ± 1	1.0	-16 ± 1	0.9	1 ± 3	0.7	$+0.09\pm0.03$	0.07
B^-	30 ± 1	0.4	-38 ± 2	0.8	-4 ± 2	1.0	-0.12 ± 0.04	0.15
B^+	-32 ± 1	0.5	39 ± 3	0.7	5 ± 2	1.0	$+0.12\pm0.04$	0.07
C^-	9 ± 1	0.7	15 ± 7	1.0	-29 ± 2	0.8	-0.12 ± 0.04	0.13
C^+	-14 ± 1	0.7	-14 ± 7	1.0	29 ± 2	0.8	$+0.10\pm0.03$	0.06
D^-	3 ± 1	0.8	-43 ± 3	0.9	7 ± 9	0.8	-0.10 ± 0.03	0.11
E^-	-20 ± 9	1.0	39 ± 9	0.7	-10 ± 1	0.8	-0.10 ± 0.03	0.12

Set (b)	δ_0	δ_1^-	δ_1^+	δ_2^-	η_2^-	$D(f)$	$P(\chi^2)$
A^-	-29 ± 3	-20 ± 2	9 ± 2	4 ± 1	0.6	-0.13 ± 0.05	0.35
A^+	31 ± 3	18 ± 2	-7 ± 2	-4 ± 1	0.5	$+0.16\pm0.05$	0.13
B^-	-3 ± 6	12 ± 2	-26 ± 2	5 ± 4	0.6	-0.20 ± 0.05	0.41
B^+	8 ± 3	-10 ± 3	26 ± 1	-4 ± 1	0.6	$+0.26\pm0.06$	0.22
C^-	21 ± 3	-21 ± 2	-3 ± 2	-22 ± 4	0.6	-0.20 ± 0.05	0.39
C^+	-22 ± 4	23 ± 1	4 ± 2	23 ± 3	0.6	$+0.24\pm0.06$	0.14

where β_K and β_P are the c.m. velocities of the K and proton, and μ_P is the proton magnetic moment in nuclear magnetons.

The ϕ_l are the differences between the nonrelativistic Coulomb phase shifts of order l and order $l=0$:

$$\phi_l = \sum_{k=1}^{l} \tan^{-1}(n/k).$$

A least-squares fitting computer program was used to find sets of phase shifts (η,α) that provided good fits to the measured angular distributions and total cross sections. Starting from a randomly chosen set of (η,α) pairs in the intervals $0<\eta<1$ and 90 deg $\leqslant\alpha\leqslant90$ deg, the computer program searched for minima in the χ^2 surface defined by

$$\chi^2 = \sum \left[\frac{d\sigma^{\text{th}}}{d\Omega}(\theta_i) - (1+\epsilon)\frac{d\sigma^{\text{exp}}}{d\Omega}(\theta_i)\right]^2 \bigg/ (\Delta_i)^2$$

$$+ \frac{[\sigma_T^{\text{th}} - \sigma_T^{\text{exp}}]^2}{(\Delta\sigma_T)^2} + \left(\frac{\epsilon}{\Delta\epsilon}\right)^2,$$

where $\Delta\epsilon$ is the uncertainty in the normalization ϵ, of the experimental differential cross section, and Δi is the experimental uncertainty in $(d\sigma/d\Omega)\exp(\theta_i)$.

About 100 different starting points were chosen at each momentum. Those minima for which $P(\chi^2)\geqslant0.05$ were considered as acceptable and are listed in Tables V and VI. The real part of the forward-scattering amplitude calculated for each solution is also given in these tables.

The acceptable phase-shift solutions that were found for each of the sets (a), (b), and (c) are given in Tables V and VI. There is a small chance that other solutions having $P(\chi^2)\geqslant0.05$ exist; all of the solutions given were found several times, starting from different initial sets of phase shifts. The main features of these solutions may be summarized as follows:

(i) Independent of which class of solutions is preferred, the data at both 970 and 1170 MeV/c favor
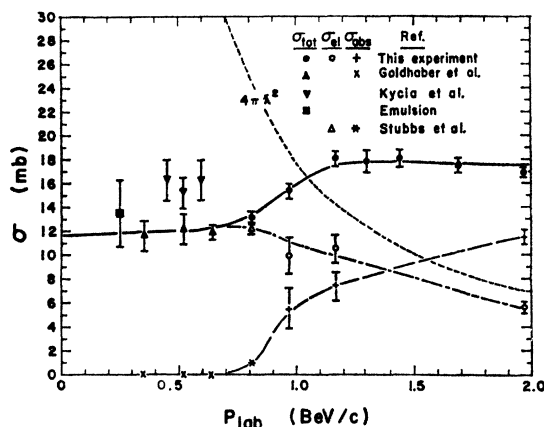

FIG. 6. The K^+-p total, elastic, and inelastic cross sections in the momentum range $P_{\text{lab}}=0$ to 2 BeV/c. The curves drawn through the measured cross sections are not derived from a theoretical model.

constructive nuclear-Coulomb interference. This implies a repulsive K^+-p force, in agreement with observations at lower momenta.

(ii) Although the various solutions in each of the sets (a), (b), and (c) predict quite different phase shifts, they lead to a more or less stable estimate of the magnitude of the real part of the forward-scattering amplitude.

(iii) The phase shift set (b), which has one less parameter to be determined than set (a), provides better fits to the 970-MeV/c data than set (a). This can be interpreted as evidence in favor of the hypothesis that $N^*(3/2,3/2)$ production is the dominant inelastic process in K^+-p scattering at 970 MeV/c.

(iv) Solutions for the 1170-MeV/c data were found for all three of the phase-shift sets. Thus we are able to say only that our results are consistent with K^*

Table VI. Phase-shift solutions found at 1170 MeV/c.

Set (a)	δ_0	η_0	δ_1^-	η_1^-	δ_1^+	η_1^+	$D(f)$	$P(\chi^2)$
A^-	-33 ± 2	1.0	-10 ± 6	0.8	4 ± 1	0.2	-0.19 ± 0.09	0.22
A^+	43 ± 2	0.8	5 ± 1	0.6	-9 ± 5	0.4	$+0.08\pm0.08$	0.07
B^-	74 ± 1	0.2	-30 ± 3	0.6	-14 ± 3	0.8	-0.19 ± 0.09	0.21
C^-	-3 ± 1	0.2	-64 ± 4	0.3	-15 ± 1	0.9	-0.20 ± 0.09	0.22
C^+	12 ± 5	0.2	55 ± 4	0.6	11 ± 2	0.8	$+0.22\pm0.10$	0.08
D^-	-9 ± 1	0.3	1 ± 5	1.0	-39 ± 1	0.5	-0.18 ± 0.10	0.21
D^+	13 ± 1	0.4	-1 ± 3	1.0	43 ± 2	0.4	$+0.17\pm0.10$	0.10

Set (b)	δ_0	δ_1^-	δ_1^+	δ_2^-	η_2^-	$D(f)$	$P(\chi^2)$
A^-	-26 ± 7	-28 ± 1	4 ± 5	-7 ± 5	0.3	-0.26 ± 0.05	0.25
A^+	23 ± 4	29 ± 1	-1 ± 4	11 ± 9	0.2	$+0.28\pm0.06$	0.05
B^-	-11 ± 9	-28 ± 2	1 ± 6	-31 ± 9	0.2	-0.25 ± 0.09	0.24
B^+	6 ± 2	34 ± 6	6 ± 3	22 ± 9	0.2	$+0.30\pm0.09$	0.06

Set (c)	δ_0	η_0	δ_1^-	δ_1^+	δ_2^-	η_2^-	$D(f)$	$P(\chi^2)$
A^-	-32 ± 10	0.6	6 ± 2	-25 ± 3	10 ± 3	0.6	-0.20 ± 0.08	0.15
B^-	-11 ± 10	0.2	-38 ± 8	-2 ± 4	1 ± 7	0.6	-0.19 ± 0.09	0.27
B^+	3 ± 10	0.1	36 ± 6	-1 ± 3	2 ± 3	0.5	$+0.21\pm0.10$	0.12
C^-	2 ± 4	0.8	-30 ± 5	2 ± 3	-30 ± 2	0.3	-0.20 ± 0.07	0.28
D^-	-41 ± 10	0.5	-29 ± 2	6 ± 2	-5 ± 3	0.5	-0.18 ± 0.08	0.27
D^+	20 ± 10	0.7	32 ± 1	-4 ± 1	3 ± 1	0.3	$+0.19\pm0.10$	0.13
E^-	-13 ± 2	0.3	29 ± 3	-9 ± 2	12 ± 2	0.4	-0.21 ± 0.08	0.12

TABLE VII. Best values found for the optical-model parameters used in fitting the angular distribution at 1970 MeV/c.

Case	Remarks	$\langle \rho^2 \rangle^{1/2}$	σ_0 (mb)	$|D(F)|$	$P(\chi^2)$
(i)	All points for which $\cos\theta^* > 0.85$, excluding spark-chamber point at $\cos\theta^* = 0.92$	0.55±0.15	3.6±0.2	0.20±0.06	0.35

Case	Remarks	$\langle \rho^2 \rangle^{1/2}$	σ_R (mb)	σ_I (mb)	$|D(F)|$	$P(\chi^2)$
(ii)	Excluding spark chamber point at $\cos\theta^* = 0.92$	0.47±0.04	3.26±0.22	0.04±0.22	0.10±0.11	0.15

and/or N^* production being the dominant inelastic process at 1170 MeV/c.

(v) All of the solutions found at both momenta imply that the S-wave phase shift is decreasing with increasing energy and the P-wave and/or D-wave phase shifts are increasing with energy.

3.2 The 1970-MeV/c Data

The 1970-MeV/c data are strongly suggestive of a predominant diffraction peak with a very small residuum of isotropic scattering (approx 0.05 mb/sr). An expansion of the angular distribution at 1970 MeV/c as a polynomial in $\cos\theta^*$ showed that terms up to order 8 were needed. As an alternative to a phase-shift analysis (which would require the inclusion of at least G waves), an optical-model approach was made in two ways by using a "grey" refracting-disk model:

(i) $1-a = (A+iB) \exp(-\rho^2/2\alpha^2)$,

(ii) $1-a = A \exp(-\rho^2/2\alpha^2) + iB \exp(-\rho^2/2\beta^2)$,

where a is the transmitted amplitude, and ρ is the radial coordinate measured from the center of the disk. The first choice was satisfactory in fitting the diffraction peak for $K^-\text{-}p$ scattering at the same momentum,[12] and was used in the present case to fit only the data $\cos\theta^* \geqslant 0.85$. The second form allows the imaginary and real parts of the scattering amplitude to have different "radii," and assumes that the Gaussian shape is an appropriate description for both. This model, thus, assumes that the diffraction peak is due to a rather large absorbing disk, and that the isotropic large-angle scattering arises from a central core. This form was used to fit the complete angular distribution.

In this model the elastic differential scattering amplitude is given by[14]

$$f(\theta) = ik \int_0^\infty (1-a) J_0(q\rho) \rho \, d\rho,$$

where k = particle wave number in the c.m. system, $q = 2k \sin(\theta/2)$, and $J_0(q\rho)$ = the zeroth-order Bessel function of the first kind.

[14] S. Fernbach, R. Serber, and T. B. Taylor, Phys. Rev. 75, 1352 (1949).

The elastic differential cross section is given by

(i) $d\sigma/d\Omega = k^2 A^2 \alpha^4 e^{-q^2\alpha^2} \equiv \sigma_0 e^{-q^2\alpha^2}$,

(ii) $d\sigma/d\Omega = k^2 A^2 \alpha^4 e^{-q^2\alpha^2} + k^2 B^2 \beta^4 e^{-q^2\beta^2}$

$$\equiv \sigma_I e^{-q^2\alpha^2} + \sigma_R e^{-q^2\beta^2}.$$

The total cross section for case (ii) is

$$\sigma_T = 4\pi A \alpha^2.$$

We define the rms radius of the interaction $\langle \rho^2 \rangle^{1/2}$ by analogy with the case of scattering from a "grey" refracting disk with a sharp boundary at radius R. In that case:

$$d\sigma/d\Omega = \text{const}(1 - \tfrac{1}{4}q^2 R^2 + \cdots)$$
$$= \text{const}(1 - \tfrac{1}{2}q^2 \langle \rho^2 \rangle + \cdots).$$

Expanding the expressions for $d\sigma/d\Omega$ in the present instance, we find for the coefficient of the $(-\tfrac{1}{2}q^2)$ term:

Case (i) $\langle \rho^2 \rangle = 2\alpha^2$,

Case (ii) $\langle \rho^2 \rangle = 2(A^2\alpha^6 + B^2\beta^6)/(A^2\alpha^4 + B^2\beta^4)$.

The best values found for the parameters are shown in Table VII. The magnitude of the real part of the forward-scattering amplitude thus derived is shown in Table VII for the two cases.

The values for the radius of the "diffracting disk" in either case (i) or (ii) appear to be smaller than the radius found for 2.0-BeV/c $K^-\text{-}p$ scattering,[12] viz., 0.79±0.04 F.

4. FORWARD-SCATTERING DISPERSION RELATIONS

Using the new data reported here, we have examined the forward-scattering $K\text{-}p$ dispersion relations to see (a) how well all the existing information can be described by these relations, and (b) how well the sign and magnitude of the hyperon pole term can now be estimated. The value of the pole term depends on the parity and coupling constants of the KYN systems. The basic dispersion relation for the real part of the forward-scattering amplitude may be written

$$D(\pm\omega) = [\Gamma/(\bar{\omega}\pm\omega)] + f(\pm\omega) + C, \quad (1)$$

with

$$f(\omega) = \frac{1}{\pi} \int_1^\infty \frac{A^+(\omega')}{\omega'-\omega} d\omega' + \frac{1}{\pi} \int_{\omega_{\Lambda_\pi}}^\infty \frac{A^-(\omega')d\omega'}{\omega'+\omega}.$$

TABLE VIII. Values of $D(\omega)$ and $f(\omega)$ for
K^+-p ($\omega>1$) and K^--p ($\omega<1$).

p_k	ω	$D(1/M_k)$	$f(\omega)$	Reference
520[a]	1.46	-1.20 ± 0.42	$+0.20$	Kycia et al.[b]
810[a]	1.92	-0.80 ± 0.23	$+0.28$	Stubbs et al.[c]
970[a]	2.22	-0.46 ± 0.19	$+0.26$	This experiment
1170[a]	2.56	-0.94 ± 0.44	$+0.05$	This experiment
1970	4.10	$\pm1.2\pm0.4$	-0.71	This experiment
1970	-4.10	$\pm3.3\pm0.6$	$+1.00$	Cook et al.[d]
513	-1.46	$\pm0.59\pm0.96$	$+0.79$	Tripp et al.[e]
434[a]	-1.33	0 ± 0.5	$+0.72$	Tripp et al.[e]
392[a]	-1.28	0 ± 0.6	$+0.87$	Tripp et al.[e]
387	-1.27	$\pm1.51\pm0.40$	$+0.86$	Tripp et al.[e]
350	-1.23	$\pm0.80\pm0.56$	$+0.84$	Tripp et al.[e]
293	-1.16	$\pm1.12\pm0.47$	$+1.00$	Tripp et al.[e]
212[a]	-1.09	-0.3 ± 1.1	$+0.65$	Humphrey et al.[f]
138[a]	-1.04	$+0.65\pm1.70$	-0.34	Humphrey et al.[f]

[a] These values were used to determine the parameters Γ and $D(\omega_0)$.
[b] Reference 2.
[c] Reference 4.
[d] Reference 12.
[e] Reference 18.
[f] Reference 20.

The residue Γ is assumed to arise from an "effective" pole, situated at "average" energy $\bar{\omega}=0.32M_K$. Early efforts[12,15] to evaluate this term gave inconclusive results. Both singly and doubly subtracted relations were used by these authors. Although these analyses were inconclusive, most of the authors found greater consistency with the data for negative values of Γ. It was assumed that the effective pole represented the effects of the adjacent Σ and Λ poles. It is now known that the interpretation of the effective pole is complicated by the Y_1^* resonance (and possibly other $\Sigma\pi$ or $\Lambda\pi$ resonances).

Our approach has been to try to fit all the available K^+-p and K^--p data. We have chosen a subtracted form:

$$D(\omega)-f(\omega)+f(\omega_0)=D(\omega_0)+\Gamma\left(\frac{1}{\bar{\omega}+\omega}-\frac{1}{\bar{\omega}+\omega_0}\right), \quad (2)$$

which eliminates the unknown constant C and ensures convergence of the subtracted integrals (subject to certain conditions on the asymptotic behavior of the total K^+-p and K^--p cross sections[16]). The parameter ω_0 can be chosen arbitrarily (we have taken $\omega_0=+1$, i.e., zero kinetic energy in the K^+-p system); then the equation contains only two free parameters $D_0\equiv D(\omega_0)$, and Γ. The integrals in $f(\omega)$ were evaluated as follows. Between $\omega'=1$ and 40, a smooth curve was drawn through the values of $A^\pm$ deduced from total cross-section measurements.[1–9,12,17,18] This smooth curve was

[15] P. T. Matthews and A. Salam, Phys. Rev. 110, 569 (1958); C. Goebel, ibid. 110, 572 (1958); K. Igi, Progr. Theoret. Phys. (Kyoto) 19, 238 (1958); R. Karplus, L. T. Kerth, and T. F. Kycia, Phys. Rev. Letters 2, 510 (1959).
[16] D. Amati, M. Fierz, and V. Glaser, Phys. Rev. Letters 4, 89 (1960); S. Weinberg, Phys. 124, 2049 (1961).
[17] S. Goldhaber, W. Chinowsky, G. Goldhaber, W. Lee, T. O'Halloran, T. F. Stubbs, G. M. Pjerrou, D. H. Stork, and H. K. Ticho, Phys. Rev. Letters 9, 135 (1962).
[18] O. Chamberlain, K. M. Crowe, D. Keefe, L. T. Kerth, A. Lemonick, Tin Maung, and T. F. Zipf, Phys. Rev. 125, 1696

continued into the unphysical region (ω' between $\omega_{\Lambda\pi}$ and 1) by using the Dalitz and Tuan S-wave zero-effective-range analysis[19] with the scattering lengths given recently by Humphrey and Ross.[20] (The effective pole residue deduced from this analysis was insensitive to which of the two Humphrey-Ross solutions was used.) The integrals were then evaluated numerically. For the region $\omega'>40$, we have used the results of Udgaonkar's[21] investigation of the asymptotic behavior of high-energy cross sections. The high-energy contribution to $f(\omega)-f(\omega_0)$ can be written

$$I(\omega)-I(\omega_0)=\frac{1}{\pi}\int_{40}^{\infty}\frac{(\omega^2-\omega_0^2)\omega'(A^-+A^+)}{(\omega'^2-\omega^2)(\omega'^2-\omega_0^2)}d\omega'$$

$$-\frac{1}{\pi}\int_{40}^{\infty}\frac{(\omega-\omega_0)(\omega'^2+\omega\omega_0)(A^--A^+)}{(\omega'^2-\omega^2)(\omega'^2-\omega_0^2)}d\omega', \quad (3)$$

where we assume

$$A^-+A^+ \rightarrow (\omega/4\pi)(F+G\omega^{\alpha-1}),$$

and

$$A^--A^+ \rightarrow (H/4\pi)\omega^\beta,$$

as $\omega(\approx k)\rightarrow\infty$.

The constants and the exponents were estimated from the data of references 6 and 9 for $\omega\gtrsim10$, and the following values were used:

$$F=23(1/M_K{}^2),$$
$$G=30(1/M_K{}^2),$$
$$H=30(1/M_K{}^2),$$

$\alpha=0.3$ to 1.0 (the results were insensitive to the value of α in this range),

$$\beta=0.25.$$

In the energy region of interest in this analysis, the values of $I(\omega)-I(\omega_0)$ turned out to be small and relatively insensitive to reasonable choices of F, G, H, α, and β.

The values of $D(\omega)$ used and the corresponding integrals $f(\omega)$ are shown in Table VIII.

It is convenient to consider Eq. (2) as representing a two-parameter family of straight lines:

$$y=\Gamma(x-x_0)+D_0, \quad (4)$$

where $x=1/(\bar{\omega}+\omega)$. The data given in the third column of Table VIII can be fitted with a straight line. The slope of this line determines the pole term Γ, and the intercept at $x=x_0$ gives the value of D_0. The experimental data and the best straight line fit (dashed line) are shown in Fig. 7. The solid curve is a plot of y vs x

(1962); M. Ferro-Luzzi, R. D. Tripp, and M. B. Watson, Phys. Rev. Letters 8, 28 (1962).
[19] R. H. Dalitz and S. F. Tuan, Ann. Phys. (N. Y.) 10, 307 (1960).
[20] W. E. Humphrey and R. R. Ross, Phys. Rev. 127, 1305 (1962).
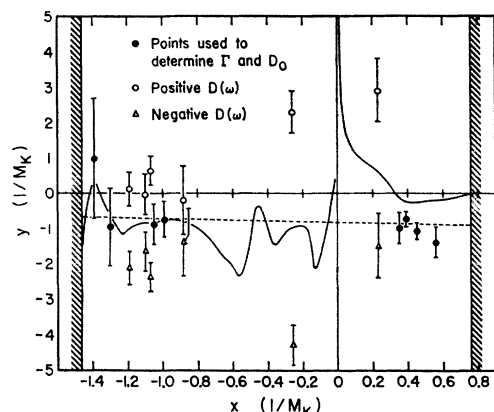[21] B. M. Udgaonkar, Phys. Rev. Letters 8, 142 (1962).

FIG. 7. The function y defined in Sec. 4 is plotted against x. The data given in Table VIII are used to calculate the values of y that are plotted as points. The solid curve is the value of y if the real part of the forward-scattering amplitude is zero for all energies.

for $D(\omega)=0$ for all ω. Contours of constant χ^2 are illustrated in Fig. 8 as a function of Γ and D_0, where

$$\chi^2=\sum_i \frac{[Z(\omega_i)-y(\omega_i)]^2}{[\epsilon(\omega_i)]^2},$$

where $Z(\omega_i)=D(\omega_i)-f(\omega_i)+f(\omega_0)$, and $\epsilon(\omega_i)$ is the error in $Z(\omega_i)$.

We have used only those values of $D(-\omega)$ for which the sign of $D(-\omega)$ has been given in determining the values of Γ and D_0 that best describe the experimental data. The results are

$$\Gamma=-0.12\pm0.32,$$

$$D_0=\quad 0.9\pm0.2(1/M_K),$$
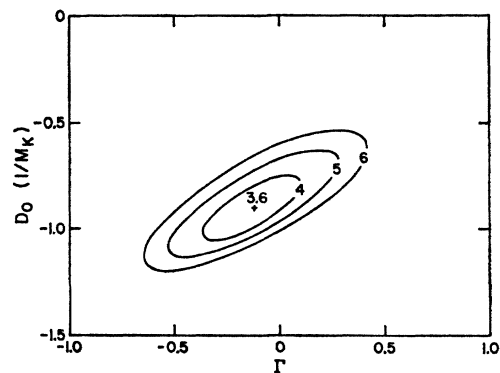
$$P(\chi^2)=0.70.$$

FIG. 8. Contours of constant χ^2 as functions of the two parameters to be determined by the fitting procedure.

Apart from one point (at $x=-0.2$), which is between 2 and 3 standard deviations away, Fig. 7 shows that reasonable linear fits can be made to the data. However, the data are still much too poor (particularly at low energies for K^--p scattering) to be able to establish definitely the sign of the pole term. It is interesting to note that if the sign of some of the low-energy K^- points could be established, the value of the slope of the straight line, and thus the pole residue, could be much better determined.
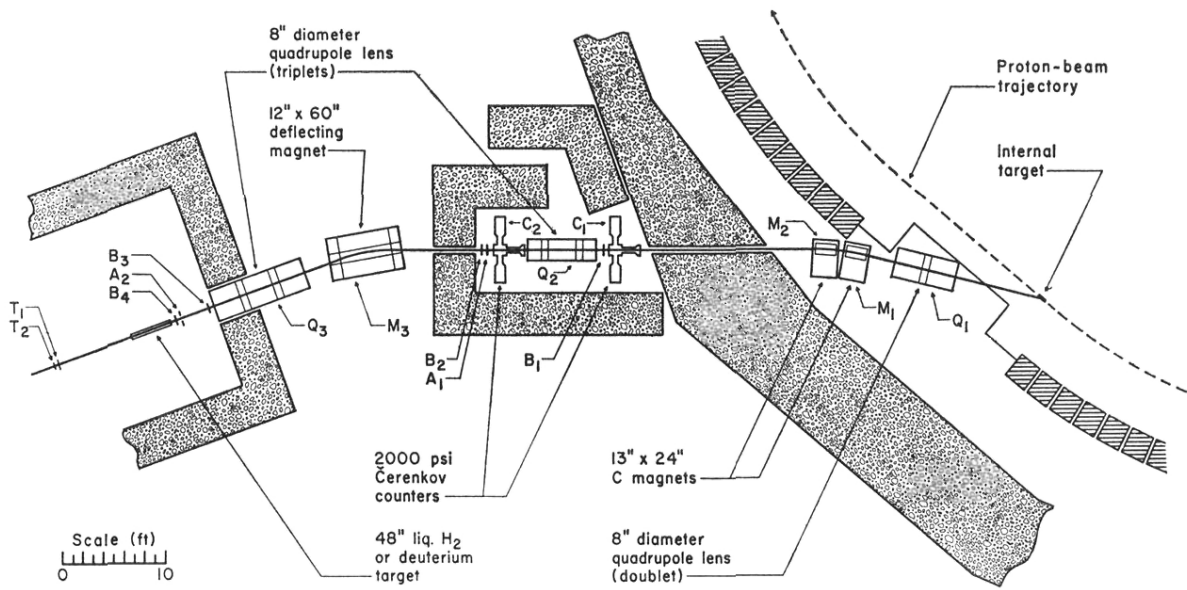
ACKNOWLEDGMENTS
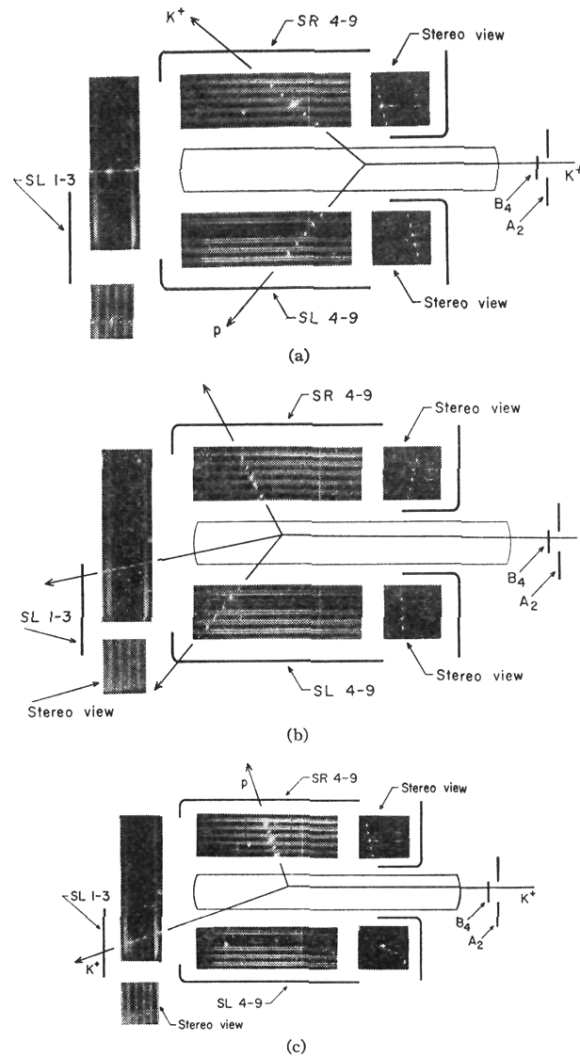
FIG. 1. Layout of K^+ beam apparatus.

FIG. 4. Composites made from typical spark-chamber photographs. (a) Elastic "side-side" scatter; (b) Inelastic scatter; (c) Elastic "front-side" scatter.